Title

Rarefaction-singular shock dynamics for conserved volume gravity driven particle-laden thin film

Permalink

https://escholarship.org/uc/item/86j6g8hv

Authors

Wang, L
Mavromoustaki, A
Bertozzi, AL
et al.

Peer reviewed

L. Wang, A. Mavromoustaki, A. L. Bertozzi, G. Urdaneta, and K. Huang

---

Articles you may be interested in

Rarefaction-singular shock dynamics for conserved volume gravity driven particle-laden thin film

L. Wang,[a] A. Mavromoustaki, A. L. Bertozzi, G. Urdaneta, and K. Huang
*Department of Mathematics, University of California Los Angeles, 520 Portola Plaza,
Los Angeles, California 90095, USA*

We employ a recently proposed model [Murisic *et al.*, "Dynamics of particle settling and resuspension in viscous liquids," J. Fluid. Mech. **717**, 203–231 (2013)] to study a finite-volume, particle-laden thin film flowing under gravity on an incline. For negatively buoyant particles with concentration above a critical value and buoyant particles, the particles accumulate at the front of the flow forming a particle-rich ridge, whose similarity solution is of the rarefaction-singular shock type. We investigate the structure in detail and find that the particle/fluid front advances linearly to the *leading order* with time to the one-third power as predicted by the Huppert solution [H. E. Huppert, "Flow and instability of a viscous current down a slope," Nature **300**, 427–419 (1982)] for clear fluid (i.e., in the absence of particles). We also explore a deviation from this law when the particle concentration is high. Several experiments are carried out with both buoyant and negatively buoyant particles whose results qualitatively agree with the theoretics. © *2015 AIP Publishing LLC.*
[http://dx.doi.org/10.1063/1.4913851]

I. INTRODUCTION

Similarity solutions have been shown to describe the evolution of thin-film equations for viscous free surface flow, which find widespread application in fluid dynamics problems. One of the earlier examples of similarity solutions in thin films is given by Huppert[1] for the flow of a constant volume of viscous fluid down a constant slope. A more complicated example takes the form of a rarefaction-undercompressive shock for the case of thermally driven films opposed by gravity.[2] Recently, there has been a lot of interest in understanding particle-laden, thin-film flows. Mixtures of particles in viscous liquid, despite their wide range of industrial and geophysical applications,[3,4] have received far less attention than homogeneous flows[1,5] and granular flows.[6,7] Recent work on fluid particle mixtures has resulted in the derivation of a quantitatively accurate dynamic mathematical model for such flows.[8] This model takes the form of a 2×2 system of conservation laws. However, analysis of that model is needed to develop general predictive theories for such flows. One class of problems that is not well-studied are similarity solutions for constant volume thin film slurries. This paper develops such a theory and compares directly with laboratory experiments. Prior theoretical work on this model focused on the Riemann problem[9,10]—which arises from a constant flux assumption rather than constant volume, coupled to a jump discontinuity such as that which arises in the case of the initial mixture released from a gate. This paper complements that literature by examining the constant volume problem—which is more relevant to typical experimental scenarios and which necessarily builds on the theory of the Riemann problem. (We use this nomenclature because of its simplicity at describing the relevant model problem.)

We briefly review some of the historical work on this problem and how it relates to this paper. For gravitational transport of particles on an inclined surface within a thin film of viscous oil,

---

[a] Author to whom correspondence should be addressed. Electronic mail: liwang@math.ucla.edu

27, 033301-1

the authors in Refs. 11 and 12 first derived a lubrication model considering the effects of gravity, capillarity, and hindered settling. Last year, a major breakthrough was made in Ref. 8 by adding shear-induced migration effects for particles in the model, successfully capturing the three distinct regimes observed in experiments. The three regimes are referred to as "settled," where the particles settle to the substrate with clear fluid flowing over them; "ridged," where the particles accumulate at the front of the flow; and "well-mixed," which is a transient, intermediate regime (see Refs. 8 and 13 for more details). For slurries with neutrally buoyant particles, only the "ridged" regime is observed experimentally. More recently, experiments were carried out[14] to investigate the bidisperse slurries composed of negatively buoyant particles, with one species being heavier than the other. There, the authors concluded that, in the "settled" regime, there exists stratification of particles by densities, due to the dominant gravitational effects. With the variation of experimental parameters (such as inclination angle and particle volume concentration), our goal is to study the macroscopic flow features. Among them, the front position is of paramount importance as it yields insight into the behavior of the various flow patterns. In Ref. 15, extensive experiments were carried out with qualitative trends suggesting that, although the presence of particles affects the geometry of the propagating front significantly, the measured average position versus time shows self-similar behavior as observed by Huppert.[1] The paper[16] develops a similarity solution theory for the earlier model in Refs. 11 and 12; however, the solutions developed do not agree with experiments because the critical physics of shear-induced migration is neglected from the earlier models. This paper fills this gap in the literature, developing the appropriate similarity solution theory for the newer class of conservation laws resulting in quantitatively different solutions that better match experimental data. In addition, very recent experiments have been conducted for neutrally buoyant particles[17] over a wide range of system parameters such as the particle concentration and the incline of the slope. The authors address the role of the particle migration on the shape of the velocity profile as well as the good performance of the lubrication theory in predicting the front position.

In the current paper, we focus on the recent model in Ref. 8, which draws inspiration from the work of Refs. 13 and 18. The model contains an equilibrium system in the wall normal direction accounting for the particle settling and shear induced resuspension, and a dynamics system (2×2 system of conservation law) describing the flow along the substrate. These two systems are separated based on the disparities in the length and time scales (lubrication scaling) and linked via the flux functions in the conservation laws. Here, the particles and liquid are assumed to be noncolloidal and incompressible, respectively, and the higher order effects such as surface tension and normal component of gravity are committed. While the settled regime is carefully examined and compared with experimental data in Ref. 8, the ridged regime has much less analytical studies, especially for the conserved volume initial data, which exhibits a self-similar solution of rarefaction-*singular* shock type that has never been explored before. Unlike[16] in which the theory relies on the "well-mixed" assumption, we treat the full 2×2 system of conservation laws. We first reduce the complexity of the rarefactions by making the assumption that in the long time limit, the concentration in the rarefaction can be approximated by its value at $\xi = \frac{x}{t} = 0$ to the leading order, and recover the linear relationship between the leading shock position with time and the one-third power (see (29)). We then derive a general connection between time and the moving contact line (see (32) and Figs. 5 and 9), which shows a slight deviation from the one-third power law. As a byproduct, we show that the singular mass corresponding to the particle-rich ridge converges to a constant with an upper bound. We also carry out some experiments to verify our theory, which, as opposed to[8] that focuses on the "settled" regime, gives a first comparison of experimental data with theoretical prediction for the "ridged" case (see Figs. 12 and 13).

The rest of the paper is organized as follows. We give a mathematical formulation of the model used in this paper in Sec. II. In Sec. III, we study in detail the rarefaction-singular shock structure for the two cases: (i) for negatively buoyant particles with concentration higher than the critical value and (ii) for buoyant particles. Since the latter case lacks analysis, we summarize the properties of its equilibrium model as well as the formation of the singular shock. In Sec. IV, we discuss comparisons between experimental and theoretical results for suspensions composed of polydimethylsiloxa (PDMS) oil and small, noncolloidal particles. Concluding remarks are given in Sec. V.

II. MATHEMATICAL FORMULATION

We use a theoretical model, derived in detail in Ref. 8, to describe the spatio-temporal evolution of a slurry mixture composed of silicon oil and noncolloidal particles. This section reviews the model derived in Ref. 8. The oil is assumed to be incompressible and of density ρ_{par} and viscosity μ_{liq}, while the particles have a density of ρ_{par}. From now on, we use the subscripts *liq* and *par* to denote the liquid and particle, respectively. A schematic of the apparatus used in the experiments is shown in Fig. 1, where x is the axial flow direction, z is the direction normal to the inclined surface, and α denotes the plane angle of inclination.

The equations governing the fluid dynamics are given by the three-dimensional continuity and Stokes equations for an incompressible fluid,

$$\nabla \cdot \mathbf{u} = 0, \tag{1}$$

$$\nabla p - \nabla \cdot \left[\mu(\phi) \left(\nabla \mathbf{u} + \nabla \mathbf{u}^T \right) \right] = \rho(\phi)\mathbf{g}, \tag{2}$$

where $\rho(\phi) = [\rho_{par}\phi + \rho_{liq}(1 - \phi)]$ and ϕ is the particle volume fraction. $\mathbf{u} = (u, v, w)$, and u, v, and w represent the axial, transverse, and normal components of the slurry mixture velocity, respectively. We note that the width of the plane is considered to be infinitely wide, and hence, any transverse effects are assumed to be negligible; this results in $v = 0$. Under the specific choice of particle and liquid parameters detailed in Sec. IV, we assume the suspension is locally Newtonian, where the effective viscosity only depends on the particle volume fraction,[19]

$$\mu(\phi) = \mu_{liq}\left(1 - \frac{\phi}{\phi_{max}} \right)^{-2}. \tag{3}$$

It is noted that the viscous forces in this setting are dominant compared to inertial forces; hence, any contributions due to inertia are ignored. For the particle volume fraction, we use a transient, particle transport equation which models the flow of particles due to advection and flux gradients,

$$\phi_t + \mathbf{u} \cdot \nabla \phi + \nabla \cdot \mathbf{J} = 0, \tag{4}$$

with

$$\mathbf{J} = \mathbf{J}_{grav} + \mathbf{J}_{coll} + \mathbf{J}_{visc}, \tag{5}$$
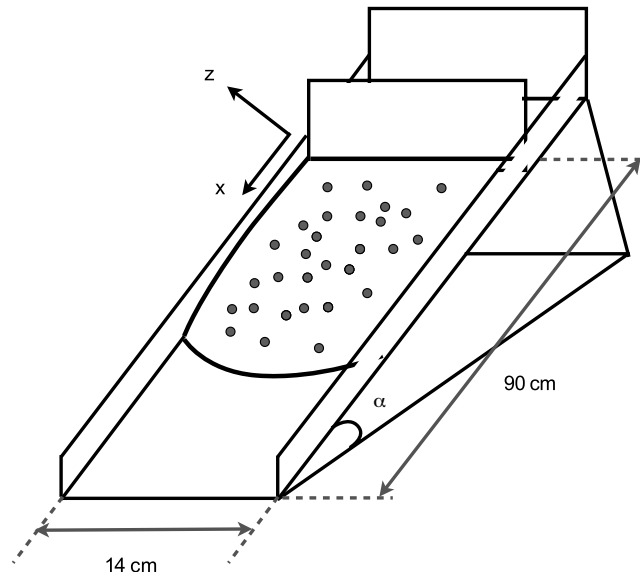

FIG. 1. Schematic plot of the geometry of the setup.

where $\mathbf{J}$ represents the total flux of particles comprised of flux due to gravity, $\mathbf{J}_{grav}$, shear-induced migration as a result of particle collisions, $\mathbf{J}_{coll}$, and viscosity gradients, $\mathbf{J}_{visc}$. The various contributions of the flux gradients are given mathematically as follows:

$$\mathbf{J}_{grav} = \frac{d^2\phi(\rho_{par} - \rho_{liq})}{18\mu_{liq}} f_s(\phi)\mathbf{g},$$

$$\mathbf{J}_{coll} = -\frac{K_c d^2}{4}\left(\phi\nabla\dot{\gamma} + \phi\dot{\gamma}\nabla\phi\right), \tag{6}$$

$$\mathbf{J}_{visc} = -\frac{K_v d^2}{4\mu}\phi^2\dot{\gamma}\mu_\phi\nabla\phi.$$

In Eq. (6), d denotes the particle diameter, $\dot{\gamma} = \frac{\partial u}{\partial z}$ is the shear rate, $f_s(\phi) = 1 - \phi$ describes hindered particle settling due to gravity, while K_c and K_v are empirical constants associated with the shear-induced migration arising from changes in the particle volume fraction and the effective suspension viscosity; these are taken as $K_c = 0.41$ and $K_v = 0.62$.[13,20] Equations (1)–(4) are solved subject to boundary conditions applied at the wall, located at $z = 0$ and at the free surface, $z = h(t, x)$. These correspond to the no-slip and no-penetration boundary condition at the wall and the tangential and normal stress balances at the free surface. Further, the kinematic boundary condition is employed to describe the motion of the fluid at the free surface,

$$\frac{D}{Dt}\left[z - h(t, x, y)\right] = 0, \tag{7}$$

where D/Dt represents the material derivative. For the particle fluxes, we impose no-flux boundary conditions at the wall and free surface for the particles,

$$\mathbf{J} \cdot \mathbf{n} = 0, \tag{8}$$

where $\mathbf{n}$ is the outward normal unit vector. To proceed, we render the above-mentioned equations dimensionless by employing the scalings below, following the work of Murisic *et al.*:[8]

$$[x] = \frac{H}{\epsilon}, \; [z] = H, \; [\phi] = 1, \; [\mu] = \mu_{liq}, \; [u] = \frac{H^2\rho_{liq}g\sin\alpha}{\mu_{liq}}, \; [t] = \frac{[x]}{[u]}, \; [p] = \frac{\mu_{liq}[u]}{\epsilon H}, \tag{9}$$

where H is the typical height of the free surface and ϵ is a small lubrication parameter given by the ratio of H to a typical length scale for the length of the plane, say L, i.e., $\epsilon \equiv H/L$. In our experiments, $H = 1$ mm and $L = 90$ cm.

To derive the reduced model,[8] we employ a separation of time scales. More specifically, we consider the fast dynamics of the concentration $\phi(t, x, z)$ profile in z-direction and a slow suspension flow down the incline since $H \ll L$. The fast process allows an averaged measure of $\phi(t, x, z)$ and velocity $u(t, x, z)$ along the normal direction and results in stationary particle fluxes in z. In the slower process, the total suspension thickness $h(t, x)$ and total number of particles $n(t, x)$ are driven by conservation laws. To apply this separation, we define the ratio between particle diameter d ($d \sim 0.25$ mm, see Table I) and H as $\eta = d/H$ which may range within $0 \le \eta \le 1$; however, to satisfy the assumptions made in the model, we demand that η does not approach the two extrema. As η approaches zero, the mixture becomes colloidal and additional fluxes are required to describe the physics. The other limit is considered impractical since, as η approaches 1, the particle diameter approaches the height of the thickness of the slurry. Therefore, to ensure that the quantity η is defined within physical limits that satisfy the theoretical model, we introduce the following distinguished limit, $\epsilon \ll \eta^2 \ll 1$ that results in the following scaling:

$$\eta^2 = \epsilon^\beta, \; 0 < \beta < 1, \tag{10}$$

which is implemented in the dimensionless version of particle transport equation (4).

Upon introducing scalings (9) and limit (10) in the relevant equation and defining $\tau = \frac{z}{h(t,x)}$ (thus $0 \le \tau \le 1$), the resulting equilibrium dynamics in z-direction are given by the solution of the

TABLE I. Experimental parameters used.

Particles	d (mm)	ρ_p (kg/m³)
Glass, negatively buoyant	0.25-0.50	2500
Glass, buoyant	0.25-0.55	640
Fluid	ν (m²/s)	ρ_l (kg/m³)
PDMS oil	10^{-3}	970

following ordinary differential equation (ODE) system:

$$\begin{cases} \left(1 + C_1 \dfrac{\phi}{\phi_{\max} - \phi}\right) \sigma \phi' + C_2 - (C_2 + 1)\phi - \rho_s \phi^2 = 0, & \text{(11a)} \\[2mm] \sigma' = -(1 + \rho_s \phi), & \text{(11b)} \\[2mm] \sigma(\tau = 1) = 0, & \text{(11c)} \\[2mm] \sigma(\tau = 0) = 1 + \rho_s \phi_0(t, x). & \text{(11d)} \end{cases}$$

Here, ϕ and σ depend on $(t, x; \tau)$, and the derivatives are with respect to τ. $\sigma(t, x; \tau)$ is the shear stress that relates to velocity u via

$$u'(t, x; \tau) = \frac{\sigma(t, x; \tau)}{\mu(\phi(t, x; \tau))}, \qquad u(x, t; 0) = 0, \tag{12}$$

where the derivative is again with respect to τ. $\phi_{\max}$ is the maximum packing fraction, and $\rho_s = \frac{\rho_{\text{par}} - \rho_{\text{liq}}}{\rho_{\text{liq}}}$, $C_1 = \frac{2(K_v - K_c)}{K_v}$, $C_2 = \frac{2\rho_s \cot \alpha}{9K_c}$ are three constants.[21] The solution of (11) is parametrized by a z−averaged particle volume fraction $\phi_0(t, x)$,

$$\phi_0(t, x) = \int_0^1 \phi(t, x; \tau) d\tau \in [0, \phi_{\max}]. \tag{13}$$

Then the slow dynamics in x−direction obeys following system of conservation laws for $h(t, x)$ and integrated volume fraction of particles $n(t, x) = h(t, x)\phi_0(t, x)$:

$$h_t + \left(h^3 f(\phi_0)\right)_x = 0, \quad n_t + \left(h^3 g(\phi_0)\right)_x = 0, \tag{14}$$

whose fluxes are obtained through

$$f(\phi_0) = \int_0^1 u(t, x; \tau) d\tau, \qquad g(\phi_0) = \int_0^1 \phi(t, x; \tau) u(t, x; \tau) d\tau. \tag{15}$$

This model applies to both buoyant and negatively buoyant particles with different parameters. For negatively buoyant particles, equilibrium system (11) has an unstable critical value ϕ_{crit} for the particle volume fraction, which leads to three different regimes observed in the experiments: settled ($\phi_0 < \phi_{\text{crit}}$), mixed ($\phi_0 = \phi_{\text{crit}}$), and ridged ($\phi_0 > \phi_{\text{crit}}$). Here, ϕ_{crit} depends on the inclination angle in the sense that smaller angle α leads to smaller ϕ_{crit}. The three regimes are shown in Fig. 2 for negatively buoyant particles. For buoyant particles, only the ridged regime appears and we will discuss it in detail in Sec. III B.

III. SIMILARITY THEORY

A. Negatively buoyant particles

In this section, we consider the flow of a mixture of oil and negatively buoyant particles described mathematically by Eqs. (11)–(14) with conserved volume initial data

$$h(0, x) = \begin{cases} h_I, & \text{for } 0 \le x \le x_I \\ 0, & \text{elsewhere} \end{cases}, \qquad \phi_0(0, x) = \phi_I, \quad n(0, x) = \phi_I h(0, x), \tag{16}$$
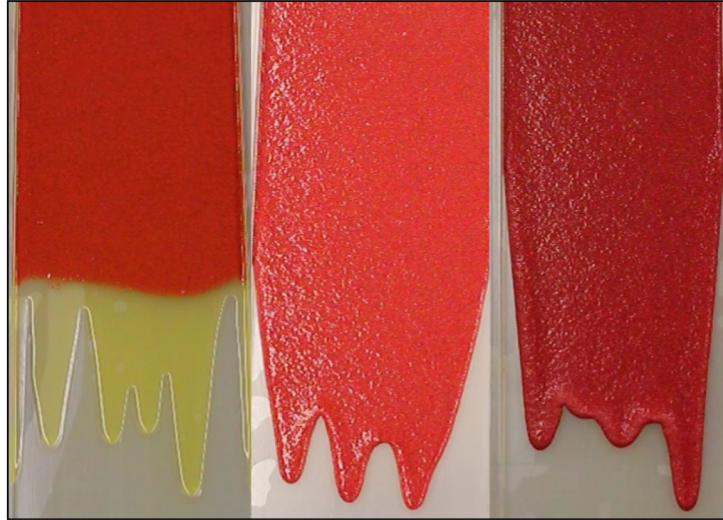
FIG. 2. Flow regime patterns emerging from a fixed volume of silicon oil laden with negatively buoyant beads. Here, the particle volume fraction is fixed at 0.40, while the plane angle of inclination is varied from 15° (left) to 30° (middle) to 45° (right) corresponding to the "settled," " well-mixed," and "ridged" regime, respectively. In the "settled" regime, clear fluid (shown in yellow) flows over the particle-rich fluid while in the "ridged" regime, the particles accumulate at the front forming a particle-rich ridge. The middle panel shows an intermediate regime where the particles remain well mixed in the fluid. The experiments were run in the Applied Mathematics Laboratory at University California, Los Angeles (UCLA).

as displayed in Fig. 3, panel (a). This can be viewed as a combination of two Riemann initial conditions, and in what follows, we named the left jump as 1-Riemann data and right jump as 2-Riemann data. Here, we focus on the high concentration case, i.e., $\phi_I > \phi_{crit}$. Then Fig. 3 shows the typical solution of h, n, and ϕ_0 at time $t = 4.5$ akin to those observed in experiments, the so-called rarefaction-singular shock.

The shock dynamics have been carefully studied in Refs. 9–11, while the analysis for rarefaction is only briefly referred to in Ref. 9. Here, we begin our discussion with the rarefaction theory. The Jacobian of hyperbolic system (14) is given by

$$J = h^2 \begin{pmatrix} 3f - \phi_0 f' & f' \\ 3g - \phi_0 g' & g' \end{pmatrix} := h^2 \tilde{J}, \qquad (17)$$

where the derivatives are with respect to ϕ_0. Denote the self-similar variable $\xi = \frac{x}{t}$, then for a given state (h_I, n_I), the sets of the states (h_r, n_r) that can be connected to (h_I, n_I) by a rarefaction curve lie on the integral curve, which is defined as $\frac{d}{d\xi}\begin{pmatrix} h_r(\xi) \\ n_r(\xi) \end{pmatrix} = \frac{\tilde{r}_i(\phi_r)}{\nabla(h_r^2 \tilde{\lambda}_i(\phi_r)) \cdot \tilde{r}_i(\phi_r)}$, $i = 1, 2$, where $\nabla = (\partial_h, \partial_n)$, $\tilde{\lambda}_i$ and $\tilde{r}_i$ are the eigenvalues and corresponding eigenvectors for $\tilde{J}$. A typical plot of the integral curve for a given right state $(h_R, n_R) = (1, 0.5)$ is displayed in Fig. 4, where the dashed curve refers to the 1-wave and solid curve refers to the 2-wave.

In general, for a 2×2 system of conservation law with Riemann initial data, one would expect two waves to connect the left and right states. However, the analysis in Ref. 10 has already shown the existence of only one singular shock for the 2-Riemann data. While Figs. 3(c) and 4 suggest that the 1-Riemann data only result in a 2-rarefaction. Henceforth, the solution for system (11)–(14) with initial data (16) only contains two waves, one for each Riemann data, namely, a 2-rarefaction following a singular shock.

More precisely, the rarefaction wave $(h_r(\xi), n_r(\xi))$ takes the form,

$$\frac{d}{d\xi}\begin{pmatrix} h_r(\xi) \\ n_r(\xi) \end{pmatrix} = \frac{\tilde{r}_2(\phi_r)}{\nabla(h_r^2 \tilde{\lambda}_2(\phi_r)) \cdot \tilde{r}_2(\phi_r)} = \frac{\tilde{r}_2(\phi_r(\xi))}{h_r(\xi)\left(2\tilde{\lambda}_2(\phi_r) - \phi_r \frac{d\tilde{\lambda}_2(\phi_r)}{d\phi_r}, \frac{d\tilde{\lambda}_2(\phi_r)}{d\phi_r}\right) \cdot \tilde{r}_2(\phi_r(\xi))}, \qquad (18)$$
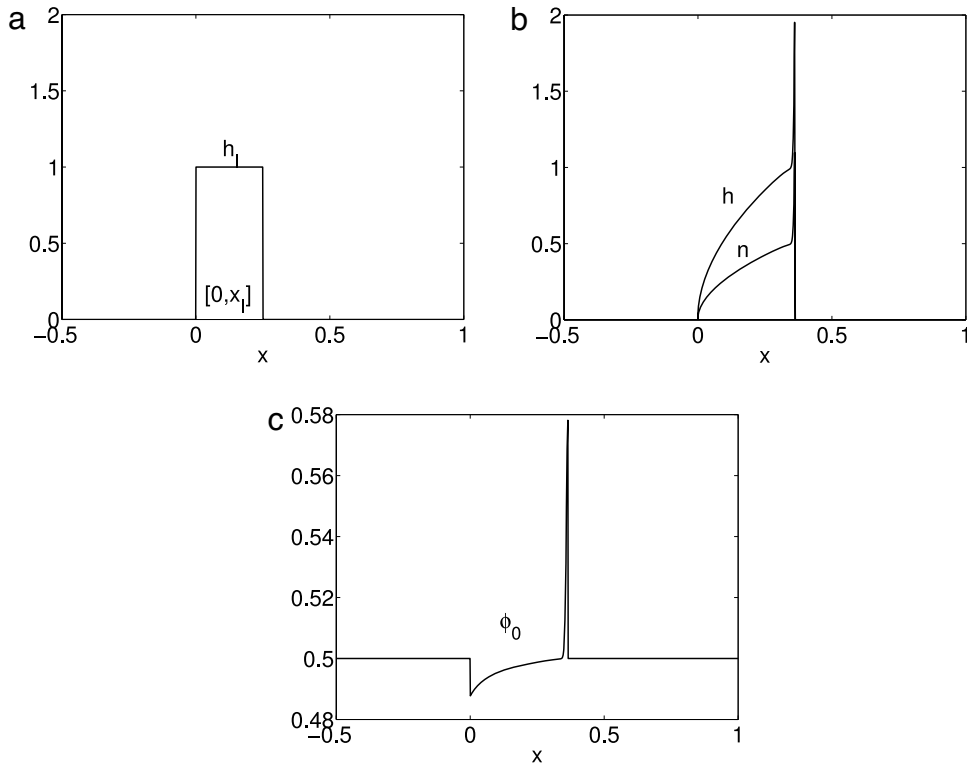
FIG. 3. (a) Initial profile for h representing a finite volume setup. Here, $x_I = 0.25$, $h_I = 1$. (b) Numerical solution for h and n at $t = 4.5$. (c) Numerical solution for ϕ_0 at $t = 4.5$. The plane angle of inclination was chosen as $\alpha = 30°$ and the initial total volume fraction was set to $\phi_I = \phi_0(0, x) = 0.5$.

with the right boundary condition

$$h_r\left(\frac{x_s}{t}\right) = h_{\text{liq}}, \quad n_r\left(\frac{x_s}{t}\right) = n_{\text{par}}, \tag{19}$$

where $x_s(t)$ denotes the singular shock position; $\tilde{\lambda}_2$ and $\tilde{r}_2$ represent the larger eigenvalue and corresponding eigenvector to matrix $\tilde{J}$, and ∇ takes (∂_h, ∂_n) as before.
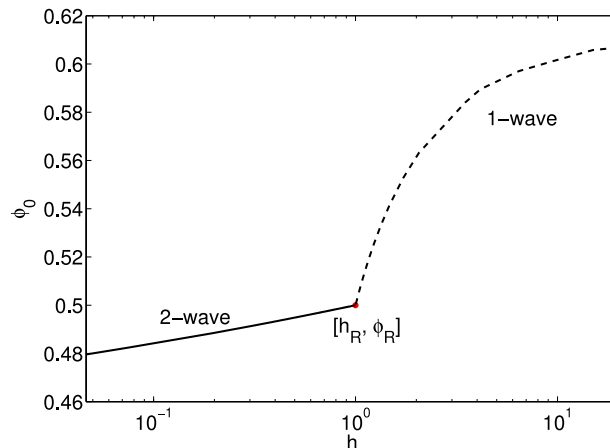

FIG. 4. Rarefaction integral curve for a given right state $(h_R, \phi_R) = (1, 0.5)$ (shown by a circle marker). The dashed curve refers to the 1-wave and the solid curve refers to the 2-wave.

We claim that the solution to (18)–(19) satisfies $h_r(0) = 0$, $n_r(0) = 0$. This is obtained by noticing that the rarefaction wave satisfies the relation $\xi = h_r^2(\xi)\tilde{\lambda}_2(\phi_r(\xi))$, with $h_r^2(\xi)\tilde{\lambda}_2(\phi_r(\xi))$ being the eigenvalue of system (14). Thus, $h_r(\xi = 0) = 0$ because $\tilde{\lambda}_2(\phi_r(\xi))$ is nonzero. Moreover, if $n_r(0) \neq 0$, we have $\phi_r(0) = \frac{n_r(0)}{h_r(0)} = \infty$, which is physically unrealistic.

Next, since $h_r(\xi)\phi_r(\xi) = n_r(\xi)$, taking derivative with respect to ξ leads to $\phi_r'(\xi)h_r(\xi) + \phi_r(\xi)h_r'(\xi) = n_r'(\xi)$, and $\phi_r(0)$ can be computed via

$$\phi_r(0) = \frac{n_r'(0)}{h_r'(0)} = \frac{\tilde{r}_2^{(2)}(\phi_r(0))}{\tilde{r}_r^{(1)}(\phi_r(0))} = \frac{\tilde{\lambda}_2(\phi_r(0)) - (3f(\phi_r(0)) - \phi_r(0)f'(\phi_r(0)))}{\frac{df}{d\phi_r}(\phi_r(0))}, \tag{20}$$

where we have used the fact that $h_r(0) = 0$ and thus, $n_r'(0) = h_r'(0)\phi_r(0)$. Here, the derivatives for h_r and n_r are with respect to ξ. $\tilde{r}_2^{(1)}$ and $\tilde{r}_2^{(2)}$ denote the one and two component for $\tilde{r}_2$, respectively. Therefore, $\tilde{\lambda}_2(\phi_r(0)) = 3f(\phi_r(0))$ and thus $\phi_r(0) = \phi_{crit}$.

To solve (18), (19) is not an easy task. Inspired by the experiments that show $x \propto t^\alpha$ with $\alpha < 1$, we observe that, in the long time limit, ξ approaches 0. Thus, we can *approximate $\phi_r(\xi)$ by $\phi_r(0)$* to the leading order, and (18) becomes

$$\frac{dh_r(\xi)}{d\xi} \simeq \frac{1}{h_r(\xi)} \frac{\tilde{r}_2^{(1)}(\phi_r(0))}{\left(2\tilde{\lambda}_2(\phi_r(0)) - \phi_r(0)\tilde{\lambda}_2'(\phi_r(0)), \tilde{\lambda}_2'(\phi_r(0))\right) \cdot \tilde{r}_2(\phi_r(0))} := \frac{1}{h_r(\xi)}A, \tag{21}$$

$$\frac{dn_r(\xi)}{d\xi} \simeq \frac{1}{n_r(\xi)} \frac{\tilde{r}_2^{(2)}(\phi_r(0))\phi_r(0)}{\left(2\tilde{\lambda}_2(\phi_r(0)) - \phi_r(0)\tilde{\lambda}_2'(\phi_r(0)), \tilde{\lambda}_2'(\phi_r(0))\right) \cdot \tilde{r}_2(\phi_r(0))} := \frac{1}{n_r(\xi)}B. \tag{22}$$

As a result, the rarefaction shapes like

$$h_r(\xi) \simeq \sqrt{2A}\sqrt{\xi}, \qquad n_r(\xi) \simeq \sqrt{2B}\sqrt{\xi}. \tag{23}$$

As already studied in Ref. 10, in the presence of the singularity at the wave front, the mass of the mixture and particles (h and n) accumulate in the singular region, and the accumulation rate satisfies the generalized Rakine-Hugoniot condition.[22] That is, if we define the singular mass as

$$M_h(t) = \int_{|x-st|<\delta} h(t,x)dx, \quad M_n(t) = \int_{|x-st|<\delta} n(t,x)dx, \tag{24}$$

with s denoting the shock speed, their growth rate satisfies

$$\frac{dM_h}{dt} = s(h_R - h_L) - \left[h_R^3 f\left(\frac{n_R}{h_R}\right) - h_L^3 f\left(\frac{n_L}{h_L}\right)\right], \quad \frac{dM_n}{dt} = s(n_R - n_L) - \left[h_R^3 g\left(\frac{n_R}{h_R}\right) - h_L^3 g\left(\frac{n_L}{h_L}\right)\right]. \tag{25}$$

Now, using the conservation of mass, we have

$$t\int_0^{\frac{x_s}{t}} \sqrt{2A}\sqrt{\xi}d\xi + M_h(t) = h_I x_I, \tag{26}$$

$$t\int_0^{\frac{x_s}{t}} \sqrt{2B}\sqrt{\xi}d\xi + \phi_{\max}M_h(t) = \phi_I h_I x_I. \tag{27}$$

Here, we make use of the fact that the singular mass in n and h satisfy the relationship $M_n(t) = \phi_{\max}M_h(t)$. As explained in Ref. 10, this can be realized either by the asymptote theory or the experimental observations that the particles pile up very tightly in the ridge regime. Notice that when $\phi_r(0) = \phi_{\text{crit}}$, the 2-eigenvalue and 2-eigenvector are $\lambda_2 = 3f(\phi_{\text{crit}})$, $r_2 = (1\ \phi_{\text{crit}})^T$. Therefore, $B = \phi_{\text{crit}}^2 A$, and the following relations are satisfied:

$$M_h(t) = \frac{(\phi_I - \phi_{\text{crit}})h_I x_I}{\phi_{\max} - \phi_{\text{crit}}}, \quad x_s = \left(\frac{(\phi_{\max} - \phi_I)h_I x_I}{\frac{2}{3}\sqrt{2A}(\phi_{\max} - \phi_{\text{crit}})}\right)^{\frac{2}{3}} t^{\frac{1}{3}} := C_s^0 t^{\frac{1}{3}}. \tag{28}$$
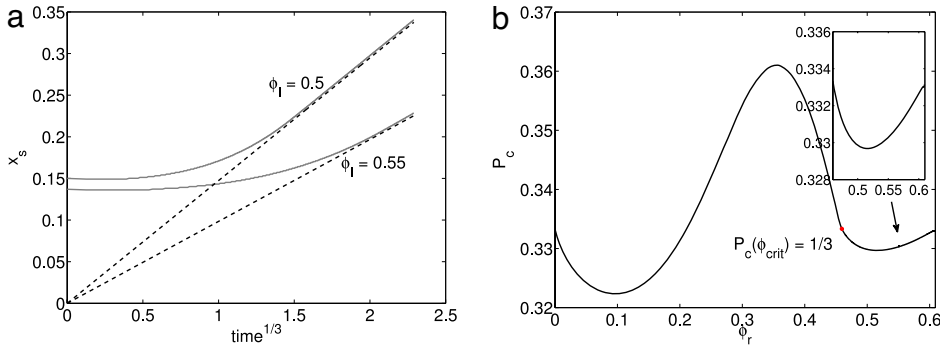
FIG. 5. Negatively buoyant particles. (a) Plots of shock wave front x_s versus time$^{1/3}$ for different concentrations $\phi_I =$ 0.5, 0.55. Grey solid lines: numerical simulation of (14). Black dash lines: slope calculated from (28). (b) Plots of P_c in (32). The plane angle of inclination was chosen as $\alpha = 30°$, and the initial data for (a) and (b) are $x_I = 0.15$, $h_I = 1$.

Then from (21), one see that $A = \frac{1}{6f(\phi_{\text{crit}})}$, and $f(\phi_{\text{crit}}) = \frac{1}{3}(1 + \rho_s \phi_{\text{crit}})\left(1 - \frac{\phi_{\text{crit}}}{\phi_{\max}}\right)^2$ by solving (11) and (12) with $\phi(\tau) \equiv \phi_{\text{crit}}$. Henceforth, further simplification of (28) leads to

$$x_s = \left[(1 + \rho_s \phi_{\text{crit}})\left(1 - \frac{\phi_I}{\phi_{\max}}\right)^2 \frac{9 h_I^2 x_I^2}{4}\right]^{\frac{1}{3}} t^{\frac{1}{3}}. \tag{29}$$

As written, Eq. (29) simply states that in the long time limit, the shock front advances proportional to the time$^{\frac{1}{3}}$, which is a reminiscent of Huppert's formulae for the clear fluid.[1]

In fact, if we assume the suspension stay *well-mixed* for all time with concentration ϕ_I, then a direct extension of Huppert's formula implies

$$x_s = \left[(1 + \rho_s \phi_I)\left(1 - \frac{\phi_I}{\phi_{\max}}\right)^2 \frac{9 h_I^2 x_I^2}{4}\right]^{\frac{1}{3}} t^{\frac{1}{3}}. \tag{30}$$

Then a comparison of (29) and (30) suggests that the effects of particle settling and resuspension slow down the advancing flow a little bit. Another observation is that the coefficient in (29) decreases as ϕ_I increases, which is consistent with the experimental results discussed by Ward *et al.*[15] Fig. 5(a) plots the shock wave front versus time$^{\frac{1}{3}}$, where the solid line is obtained by solving the system of conservation laws (14) and the dashed line has a slope given by (29). We observe that (29) is somewhat underestimated due to approximation (23) being only accurate to the leading order.

As a matter of fact, we can have a more precise result without doing the approximation. Recall that for given left and right states (h_L, ϕ_L) and (h_R, ϕ_L), the singular shock speed follows:[10]

$$s = \frac{(h_L^2 + h_R^2 + h_L h_R)(\phi_{\max} f(\phi_L) - g(\phi_L))}{\phi_{\max} - \phi_L}. \tag{31}$$

Then in our case with $h_L = h_r(\xi)$, $\phi_L = \phi_r(\xi)$, and $h_R = 0$, we have

$$\frac{dx_s(t)}{dt} = \frac{h_r^2(\phi_{\max} f(\phi_r) - g(\phi_r))}{\phi_{\max} - \phi_r} = \frac{\phi_{\max} f(\phi_r) - g(\phi_r)}{(\phi_{\max} - \phi_r)\tilde{\lambda}_2(\phi_r)} \frac{x_s}{t} := P_c \frac{x_s}{t}, \tag{32}$$

where we have used the relation $\xi = \frac{x}{t} = h_r^2(\xi)\tilde{\lambda}_2(\phi_r(\xi))$. This implies $x_s(t) \propto t^{P_c}$, where P_c is given in Fig. 5. Here, one observes that P_c is around $\frac{1}{3}$ for $\phi_0 > \phi_{\text{crit}}$, which validates the approximation in the leading order. Then, the conservation of mass

$$t \int_0^{\frac{x_s}{t}} h_r(\xi) d\xi + M_h(t) = h_I x_I, \quad t \int_0^{\frac{x_s}{t}} n_r(\xi) d\xi + \phi_{\max} M_h(t) = h_I x_I \phi_I$$

gives rise to $h_r(\xi) \propto \xi^\alpha$ and $n_r(\xi) \propto \xi^\alpha$ with $\alpha = \frac{P_c}{1-P_c}$. Moreover, we obtain the form of the singular mass, $M_h(t) = \frac{\phi_I - \phi_r}{\phi_{\max} - \phi_r} h_I$ with $\phi_r \in [\phi_{\rm crit}, \phi_I]$, which implies the following upper bound:

$$0 \le M_h(t) \le h_I \min \left\{ \frac{\phi_I - \phi_{\rm crit}}{\phi_{\max} - \phi_{\rm crit}}, \phi_I \right\}. \tag{33}$$

B. Buoyant particles

In this section, we consider suspensions with buoyant particles. The model remains the same as in (11)–(14) but with the density for particles smaller than liquid, and thus $\rho_s = \frac{\rho_{par} - \rho_{liq}}{\rho_{liq}} < 0$. Then the two constants in (11) have signs $C_1 = \frac{2(K_v - K_c)}{K_v} > 0$ and $C_2 = \frac{2\rho_s \cot\alpha}{9K_c} < 0$. Notice that contrary to the negatively buoyant case, we have for $\phi \in [0, \phi_{\max}]$, $\rho_s \phi^2 + (C_2 + 1)\phi - C_2 > 0$ for any angle $\alpha \in [0, 90°]$; thus, there is no critical point and particles tend to the front to form the particle-rich ridge. Figure 6 gives a typical plot of particle volume fraction ϕ, shear stress σ, and suspension velocity u for $\alpha = 30°$. It is interesting to point out that the shape of velocity u is blunting in contrast to the parabolic profile for homogeneous Newtonian fluids, which is in good agreement with the experimental observation in Ref. 17. Figure 7 compares the fluxes $f(\phi_0)$ and $g(\phi_0)$ for buoyant and negatively buoyant particles for $\alpha = 30°$. One noticeable difference lies in the panel (c), where we plot $\frac{g(\phi_0)}{\phi_0 f(\phi_0)}$ versus ϕ_0. This ratio indicates the relative speed of particles and bulk fluid. Namely, if it is greater than one, then fluid flows faster than particles and leads to ridged regime; while if it is less than one, it results in a settled regime. Then as shown in panel (c) in Fig. 7,
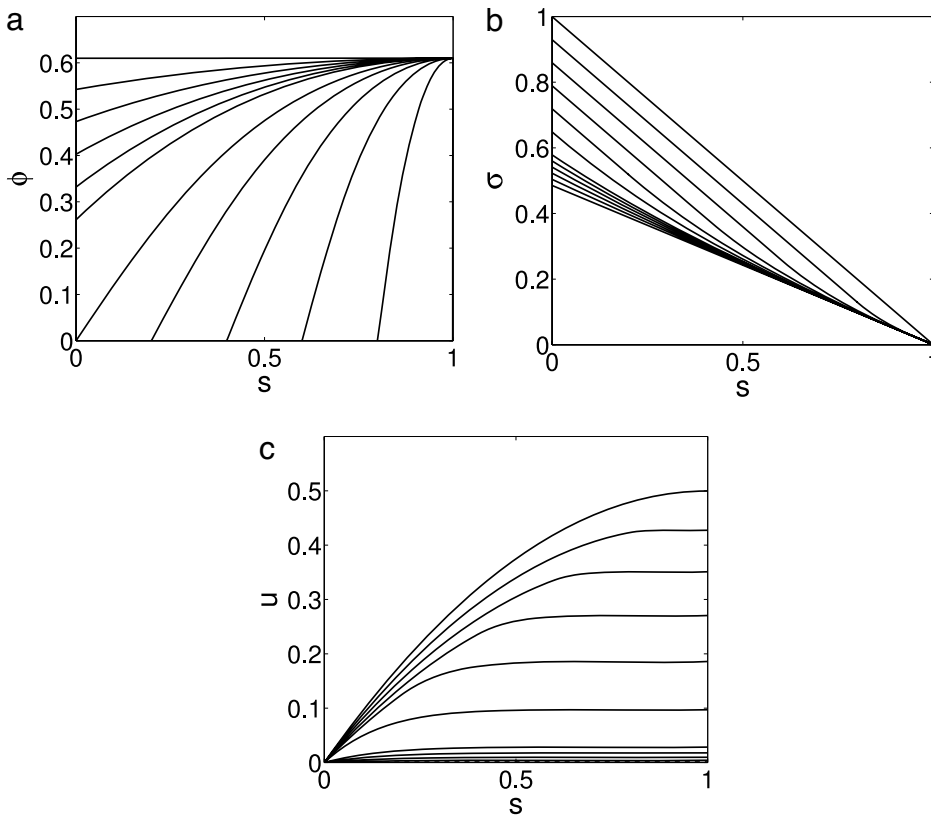

FIG. 6. Plots of solutions to (11) with buoyant particles for $\alpha = 30°$. The horizontal axis represents the τ variable. Different curves refer to different data ϕ_0. Panel (a): particle volume fraction ϕ. ϕ_0 is decreasing from top to bottom, left to right. Panel (b): shear stress σ, ϕ_0 is decreasing top-down. Panel (c): suspension velocity u, ϕ_0 is decreasing bottom-up.
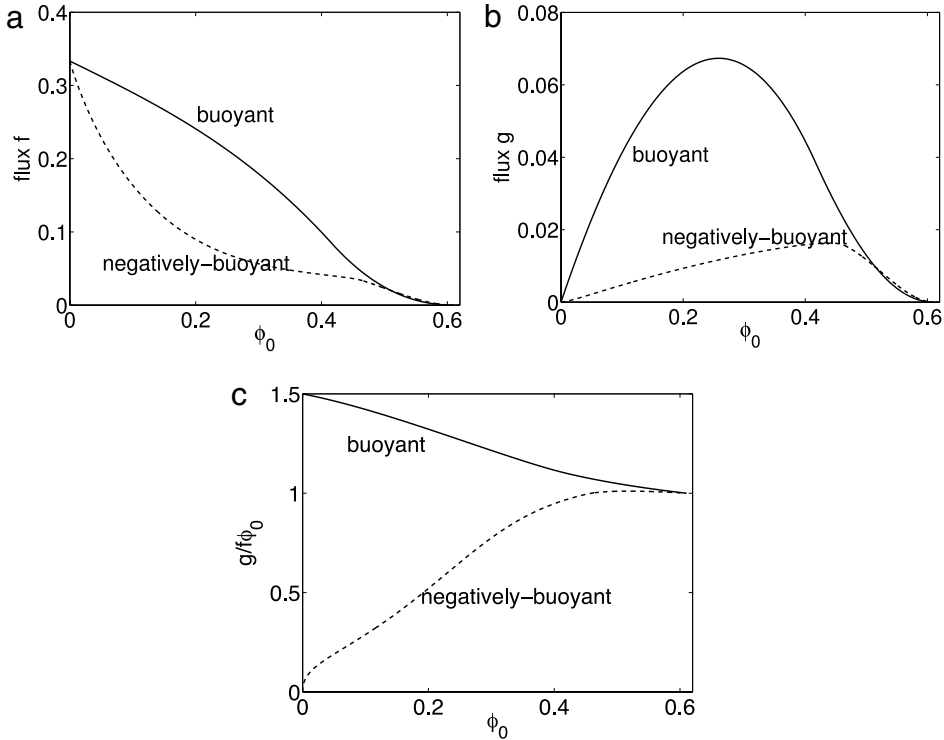
FIG. 7. Fluxes f [panel (a)] and g [panel (b)] for buoyant and negatively buoyant cases. Plots of $g/(f\phi_0)$ [panel (c)] for both buoyant and negatively buoyant cases. The plane angle of inclination is set to $\alpha = 30°$.

such ratio in the buoyant case stays above one, and for the negatively buoyant case, it transits from less than one to larger than one at the critical point, just as we expected.

1. Singular shock formation

Since the formation of the singular shock for buoyant particles is similar to the negatively buoyant case with high particle concentration, the results in Ref. 10 can be applied here with a slight change to fit the buoyant parameters. Here, it is customary to give a brief explanation of singular shock, and a grasp of the following simple statements will suffice our purpose.
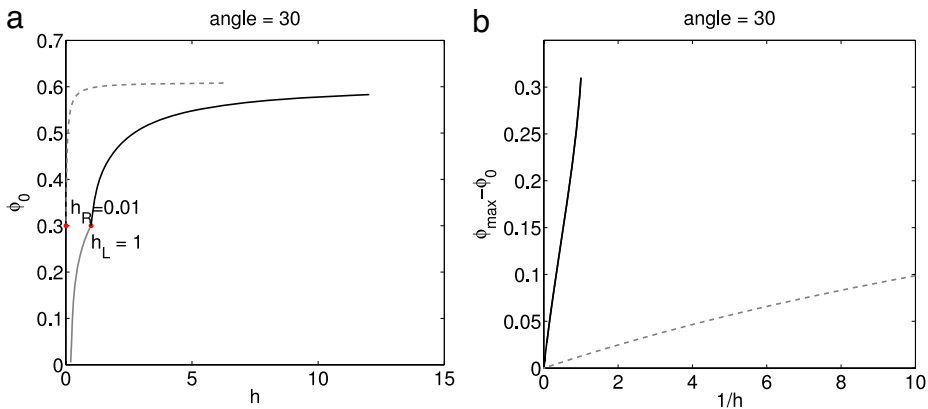

FIG. 8. (a) The entropy-satisfying shocks connecting the left state $(h_L, \phi_L) = (1, 0.3)$ (black curves) and right state $(h_R, \phi_R) = (0.01, 0.3)$ (grey dashed curves). (b) Replotted Hugoniot loci from panel (a) with vertical axis representing $\phi_{max} - \phi_0$ and horizontal axis representing $\frac{1}{h}$. The plane angle of inclination is $\alpha = 30°$.
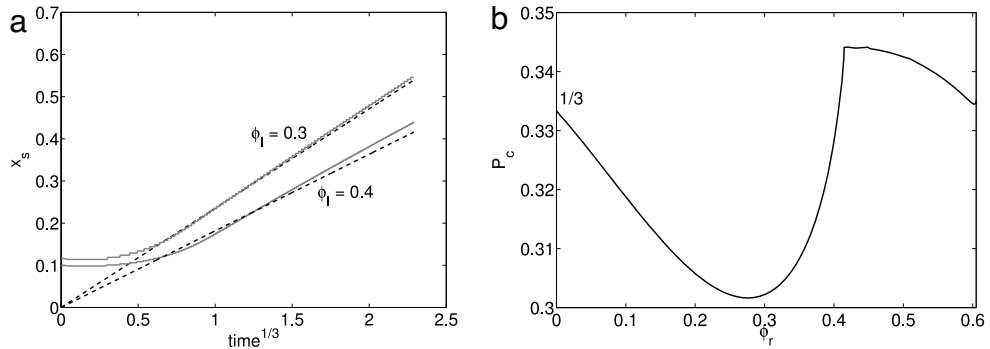
FIG. 9. Buoyant particles. (a) Plots of singular shock front x_s versus time$^{1/3}$ for different values of concentration: $\phi_I = 0.3$, 0.4. Grey solid lines: numerical simulation of (14); black dash lines: slope calculated from (28). (b) Plots of P_c in (32) for the buoyant case. Again, $\alpha = 30°$, and the initial data for (a) and (b) are $x_I = 0.15$, $h_I = 1$.

Given a left state (denoted as (h_L, ϕ_I)), first compute B and θ via equations (4.6) and (4.7) in Ref. 10, then we can define a threshold for the thickness of the right state as $h_R^* = h_L \frac{1 - \cos\frac{\theta}{3} + \sqrt{3}\sin\frac{\theta}{3}}{1 + 2\cos\frac{\theta}{3}}$ in the sense that for a given right state (h_R, ϕ_I), if $h_R > h_R^*$ classical double shock forms, whereas $h_R \leq h_R^*$ induces a singular shock. This is because the Hugoniot loci (the collection of states that can connect to the left and right states through a shock) for the left and right states are *asymptotically parallel* (which means they are parallel when h is sufficiently large) that fails to produce an intersection as the intermediate state for double shock. Fig. 8 displays the Hugoniot loci for left and right states $(h_L = 1, \phi_I = 0.3)$ and $(h_R = 0.01, \phi_I = 0.3)$, which clearly shows the asymptotic parallelism of them. The singular shock speed still follows (31).

2. Rarefaction-singular shock solution

By analogy with the negatively buoyant case, we first approximate $\phi_r(\xi)$ by $\phi_r(0)$ near $\xi = 0$, then we can compute $\phi_r(0)$ as in (20), and get $\phi_r(0) = 0$ in this case. A similar approach in (21)–(27) applies and yields the relationship between particle front position and time as in (28). This relation is shown in Fig. 9(a), where the black line is obtained by solving the hyperbolic conservation laws and the dashed line has the slope in (28). We can also derive the relations between time and shock position similarly using (32) but with f and g for the buoyant case. A typical plot of P_c is given in Fig. 9(b) for $\alpha = 30°$. It is again shown that P_c is in the neighborhood of $\frac{1}{3}$. As a result, the singular mass has same estimate (33).

It is also worth comparing the particle front position versus time through Eq. (29) for negatively buoyant and buoyant cases. The results are shown in Fig. 10, which qualitatively agree with the experimental results in Refs. 15 and 17. We observe that the buoyant particles are slower than the negatively buoyant ones. Moreover, the comparison with Huppert's formula (30) (this formula assumes the particles and fluid are "well-mixed") implies that in the presence of particle setting and resuspension, if the particles are negatively buoyant, the speed of the slurry mixture is slightly decreased, while on the other hand, if the particles are buoyant, the speed of the slurry mixture is increased.

IV. EXPERIMENTS

A. Procedure

In this section, we provide details of the experimental setup and procedure. A schematic of the apparatus is shown in Fig. 1; it consists of an acrylic track of length 90 cm and width 14 cm with an inclination angle, α, where the latter may be adjusted within $5° < \alpha < 80°$. In the experiments we carry out, we are interested in the flow patterns that emerge from gravity-driven slurry flows
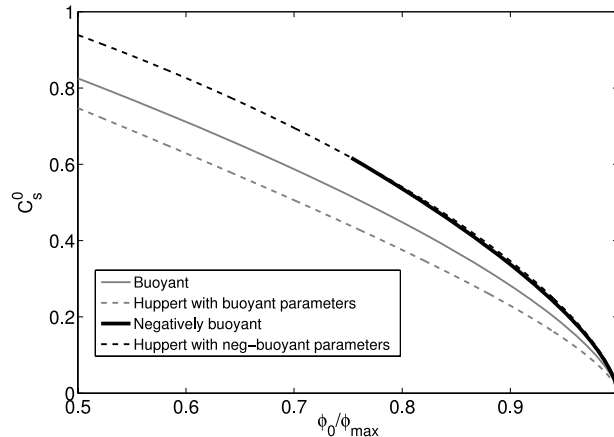
FIG. 10. Plots of C_s^0, obtained using Eq. (28) against $\frac{\phi_0}{\phi_{max}}$. For simplicity, we use $x_I = h_I = 1$ here. Grey solid curve: buoyant case; black solid curve: negatively buoyant case. Grey dashed curve: Huppert formula (30) with buoyant parameters; black dashed curve: Huppert formula with negatively buoyant parameters. Again, $\alpha = 30°$.

composed of PDMS oil and noncolloidal beads. Two types of beads are used: negatively buoyant (approximately 2.5 times heavier than the fluid) and buoyant (approximately 0.6 times lighter than the fluid). The two system parameters we are interested in varying are α and the initial particle volume fraction, ϕ_I. Slurry mixtures of 100 ml total volume are prepared for different values of ϕ_I and deposited in the reservoir with the release gate initially closed. The start of each run is marked at the point when the gate is lifted. The slurry mixture subsequently flows down the track and the motion is recorded using a digital camera until the front of the flow reaches the end of the track. The runs are repeated 2-3 times to validate the experimental results; it is noted that the patterns resulting from the same experiment were found to be very similar and a high degree of repeatability was recorded. The experimental parameters used are summarized in Table I. Similar experiments were carried out in Ref. 15, but the data there are not collected in a scale that can be compared with theory. So we redo the experiments here.

In the case of negatively buoyant particles, we observe three distinct regimes, depending on the particle volume fraction, as shown in the work of Murisic *et al.*[8,13] As discussed in Sec. III, the equilibrium model exhibits an unstable critical value for the particle volume fraction, denoted by ϕ_{crit}. While the slurry mixture starts off as "well-mixed," within $0 < \phi < \phi_{crit}$, gravitational settling dominates thus clear fluid flows over particles which settle fast to the substrate. Within $\phi_{crit} < \phi < \phi_{max}$, competition between gravitational settling and shear-induced migration leads to the particles accumulating at the front of the flow forming a particle-rich ridge. As previously discussed, the two regimes are termed "settled" and "ridged," respectively. In this section, we are interested in making comparisons between experimental and theoretical results focussing on the "ridged" regime. The reader is referred to previous work[8,13] for comparisons within the "settled" regime.

B. Comparison between experimental results and theoretical predictions

In Fig. 11, we show a series of static images of the slurry mixtures flowing down the plane with the angle of inclination fixed at $\alpha = 40°$. The pictures show a comparison between the evolution of the flow patterns for the cases of buoyant particles (pink slurry flows) and negatively buoyant particles (red slurry flows). Figure 11 depicts the flow patterns initially [panels (a), (b)], when the slurries have travelled approximately half way down the plane [panels (c), (d)] and in their fully developed patterns [panels (e), (f)]. The different times corresponding to each panel are included in the figure caption. We observe that for both particle species, the flow patterns develop in the "ridged" regime where the majority of particles accumulate at the front of the flow; hence, the particle and fluid fronts coincide. We note that for the set of system parameters shown in Fig. 11, the
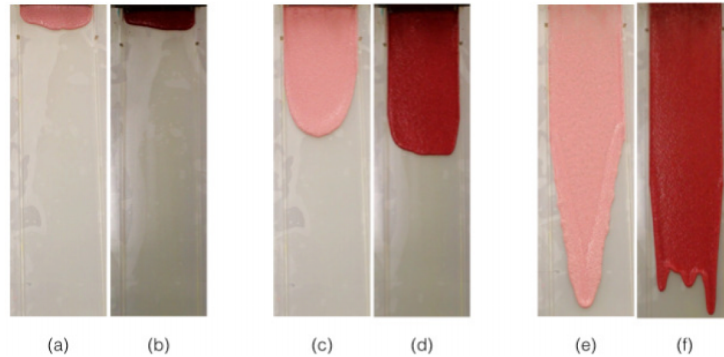
FIG. 11. Static images for buoyant (pink) and negatively buoyant (red) slurries flowing down the plane inclined at $\alpha = 40°$. The total particle concentration for both slurry mixtures is fixed at $\phi_I = 0.40$. The images of the buoyant slurry mixtures are captured at $t = 13, 125, 625$ s [shown in panels (a), (c), (e)] while the negatively buoyant slurry mixtures are captured at $t = 4, 46, 237$ s [shown in panels (b), (d), (f)].

slurry made of negatively buoyant particles traveled the same distance in approximately a third of the time.

In Figs. 12 and 13, we plot the theoretical prediction of the relationship between the fluid/particle front (i.e., the singular shock front) and time$^{1/3}$ and compare it to the experimental results for negatively buoyant and buoyant beads, respectively. Figure 12 depicts the results using negatively buoyant particles for an angle of inclination of 40° [panel (a)] and 50° [panel (b)] for $\phi_I = 0.50, 0.55$. We observe that, after an initial transient time, wherein the mixture moves from the initial well-mixed state to the "ridged" regime, the relation of the moving front with time$^{1/3}$ shows good agreement between the theoretical and experimental results. Figure 13 shows the relationship between the theoretical prediction and experimental results for buoyant particles. The experiments are carried out for two angles of inclination: 30° [panel (a)] and 40° [panel (b)] at $\phi_I = 0.30, 0.40$. As previously mentioned, in the case of buoyant particles, any ϕ_I within $0 < \phi_I < \phi_{max}$ results in the development of the "ridged" regime leading to the two fronts (liquid and particle) coinciding. We observe a longer initial transient time compared to the negatively buoyant case. At late times, while the theoretical prediction approaches the slope of the experimental results, we note that the agreement is not as good as in the results shown in Fig. 12. A possible reason for this behavior is given by the experimental images shown in Fig. 11: for the buoyant particles (pink slurry flows), we observe the presence of significant wall boundary effects. The beads advance to the front and concentrate in the middle of the
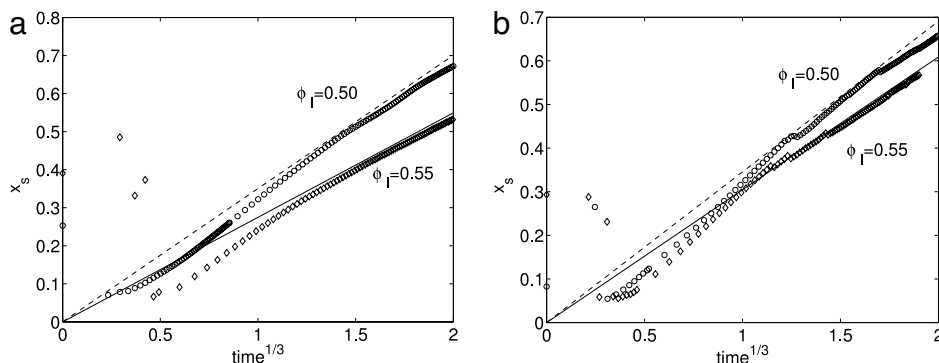

FIG. 12. Comparison of experimental results against the theoretical formula given by Eq. (29) on the relationship of the location of the front, x_s, and time$^{1/3}$. In panel (a), α is set at 40° while in (b), $\alpha = 50°$. In both panels, the particle concentration is varied from $\phi_I = 0.50$ (experiment: circle markers, theory: dashed line) to $\phi_I = 0.55$ (experiment: diamond markers, theory: solid line). For all system parameters shown, the experimentally observed flow pattern was within the "ridged" regime.
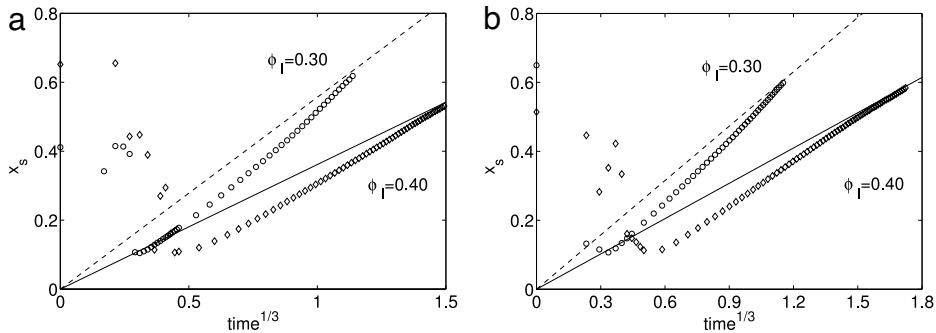
FIG. 13. Comparison of experimental results against the theoretical formula given by Eq. (29) on the relationship of the location of the front, x_s and time$^{1/3}$ for buoyant particles. The plane angle of inclination α is set at 30° [panel (a)] and 40° [panel (b)] and the particle concentration is varied from $\phi_I = 0.30$ to $\phi_I = 0.40$.

plane. Since the theoretical prediction is based on a one-dimensional model, a more uniform averaged front is expected to compare more closely to theoretical predictions. It can be observed in Fig. 11 that the averaged front of the flow in the case of negatively buoyant particles (red slurry flows) is more uniform compared to the buoyant case.

This study was concerned with a 1D model incorporating the most dominant physical forces, neglecting higher order effects such as hydrostatic and surface tension forces. A comparison of the experimental results and the theoretical prediction on the speed of the front suggests that, while the agreement is good, the inclusion of higher order effects can help improve the 1D mathematical model and, in turn, theoretical predictions. Further, taking into account, transverse effects can help explain why wall boundary effects are more prominent in the case of buoyant particles while a linear stability analysis will address questions on the shape of the front and the fingering instability observed at the contact line.

V. CONCLUDING REMARKS

This paper focuses on the "ridged" regime observed in the gravitational flow of a finite-volume, particle-laden thin film down a rectangular plane. In the case of slurries composed of negatively buoyant particles, this regime is observed experimentally at high particle concentrations and high angles of inclinations while for buoyant particles, the "ridged" regime is the dominant flow pattern. In this paper, we use a previously derived model[8] based on the lubrication approximation and the assumption that the particle distribution in the normal direction to the plane is in equilibrium.

We discuss our findings for slurries made up of both negatively buoyant particles (approximately 2.5 times heavier than the fluid) and buoyant particles (approximately 0.6 times lighter than the fluid). In both cases, the solution is described by a rarefaction-singular shock. In the long time scaling, we approximate the rarefaction wave at its leading order and find that the shock wave front moves linearly with time to the one third power. This is reminiscent of Huppert's result for clear fluid.[1] We also derive a general relationship between the moving wave front and time which reveals some deviation forms the one third power law. This coincides with the experimental observations in Ref. 15.

Next, we carry out experiments to investigate how the time-dependent relationship of the front of the flow obtained theoretically, compares against physical results. For the heavy particles, we choose particle concentrations that exceed the critical value to ensure the flow patterns are in the "ridged" regime. It is noted that all slurry runs start off from a "well-mixed" state. We carry out a series of experiments at two different angles: 40° and 50° (negatively buoyant) and 30° and 40° (buoyant) and two different particle concentrations, $\phi_I = 0.50$ and $\phi_I = 0.55$ (negatively buoyant) and $\phi_I = 0.30$ and $\phi_I = 0.40$ (buoyant). We find that, after an initial transient period, the front of the flow shows a linear relationship with time$^{1/3}$ which approaches the slope of the formula obtained theoretically. For the negatively buoyant particles, the good agreement between experiments and

theory is consistent. For the buoyant particles, we observe a longer initial transient period and, while we recover a linear relationship between x_s and time$^{1/3}$, the agreement is not as good as in the negatively buoyant case due to significant wall boundary effects.

ACKNOWLEDGMENTS

[1] H. E. Huppert, "Flow and instability of a viscous current down a slope," Nature **300**, 427–429 (1982).

[2] A. Munch and A. Bertozzi, "Rarefaction-undercompressive fronts in driven films," Phys. Fluids **11**, 2812 (1999).

[3] O. Katz and E. Aharonov, "Landslides in vibrating sand box: What controls types of slope failure and frequency magnitude relations?," Earth Planet. Sci. Lett. **247**, 280–294 (2006).

[4] A. Klar, E. Aharonov, B. Kalderon-Asael, and O. Katz, "Analytical and observational relations between landslide volume and surface area," J. Geophys. Res.: Earth Surf. **116**, F02001, doi:10.1029/2009jf001604 (2011).

[5] M. F. G. Johnson, R. A. Schluter, M. J. Miksis, and S. G. Bankofft, "Experimental study of rivulet formation on an inclined plate by fluorescent imaging," J. Fluid Mech. **394**, 339–354 (1999).

[6] H. E. Huppert, "Quantitative modeling of granular suspension flows," Philos. Trans. R. Soc., A **356**, 2471–2496 (1998).

[7] O. Pouliquen, J. Delous, and S. B. Savage, "Fingering in granular flows," Nature **386**, 816–817 (1997).

[8] N. Murisic, B. Pausader, D. Peschka, and A. L. Bertozzi, "Dynamics of particle settling and resuspension in viscous liquids," J. Fluid Mech. **717**, 203–231 (2013).

[9] A. Mavromoustaki and A. L. Bertozzi, "Hyperbolic systems of conservation laws in gravity-driven, particle-laden thin-film flows," J. Eng. Math. **88**(1), 29–48 (2014).

[10] L. Wang and A. L. Bertozzi, "Shock solutions for high concentration particle laden thin films," SIAM J. Appl. Math. **74**(2), 322–344 (2014).

[11] B. Cook, A. Bertozzi, and A. Hosoi, "Shock solutions for particle-laden thin films," SIAM J. Appl. Math. **68**, 760–783 (2008).

[12] J. Zhou, B. Dupuy, A. L. Bertozzi, and A. E. Hosoi, "Theory for shock dynamics in particle-laden thin films," Phys. Rev. Lett. **94**, 117803 (2005).

[13] N. Murisic, J. Ho, V. Hu, P. Latterman, T. Koch, K. Lin, M. Mata, and A. L. Bertozzi, "Particle-laden viscous thin-films on an incline: Experiments compared with a theory based on shear-induced migration and particle settling," Physica D **204**(20), 1661–1673 (2010).

[14] S. Lee, A. Mavromoustaki, G. Urdaneta, K. Huang, and A. L. Bertozzi, "Experimental investigation of bidensity slurries on an incline," Granular Matter **16**(2), 269–274 (2014).

[15] T. Ward, C. Wey, R. Glidden, A. E. Hosoi, and A. L. Bertozzi, "Experimental study of gravitation effects in the flow of a particle-laden thin film on an inclined plane," Phys. Fluids **21**, 083305 (2009).

[16] N. Grunewald, R. Levy, M. Mata, T. Ward, and A. L. Bertozzi, "Self-similarity in particle laden flows at constant volume," J. Eng. Math. **66**, 53–63 (2010).

[17] C. Ancey, N. Andreini, and G. Epely-Chauvin, "The dam-break problem for concentrated suspensions of neutrally buoyant particles," J. Fluid Mech. **724**, 95–122 (2013).

[18] B. Cook, "Theory for particle settling and shear-induced migration in thin-film liquid flow," Phys. Rev. E **78**, 045303 (2008).

[19] J. F. Richardson and W. N. Zaki, "The sedimentation of a suspension of uniform spheres under conditions of viscous flow," Chem. Eng. Sci. **5**, 65–73 (1954).

[20] R. J. Phillip, R. C. Armstrong, R. C. Brown, A. L. Graham, and J. R. Abbott, "A constitutive equation for concentrated suspensions that accounts for shear-induced particle migration," Phys. Fluids A **4**, 30 (1992).

[21] A. Acrivos, G. K. Batchelor, E. J. Hinch, D. L. Koch, and R. Mauri, "Longitudinal shear-induced diffusion of spheres in a dilute suspension," J. Fluid Mech. **240**, 651–657 (1992).

[22] M. Sever, *Distribution Solutions of Nonlinear Systems of Conservation Laws* (Memoirs of the American Mathematical Society, 2007), Vol. 190.